Research Square

Preprints are preliminary reports that have not undergone peer review.
They should not be considered conclusive, used to inform clinical practice,
or referenced by the media as validated information.

Wave-to-water energy balance of an S-shaped buoy and ball-screw power take-off driving small-scale batch reverse osmosis

Ammar Ahmed
South China University of Technology
Ali Azam
South China University of Technology
Zhichao Shen
shenzhichao@scut.edu.cn

South China University of Technology
Xidong Zhou
South China University of Technology
Christopher N. Mkono
South China University of Technology
Zhongliang Meng
Qufu Normal University
Jakiya Sultana
University of Miskolc
Mazedur Rahman
University of Miskolc
Touqeer Aslam
South China University of Technology
Dawood Majeed
Slovak University of Technology in Bratislava

Research Article

Keywords: Wave energy, Power take-off, Ball screw, Batch reverse osmosis, Capture width ratio, Desalination

Posted Date: November 17th, 2026

DOI: https://doi.org/10.21203/rs.3.rs-11299333/v1

License: This work is licensed under a Creative Commons Attribution 4.0 International License.
Read Full License

Additional Declarations: No competing interests reported.

Wave-to-water energy balance of an S-shaped buoy and ball-screw power take-off driving small-scale batch reverse osmosis

Ammar Ahmed [1, †], Ali Azam [1, †], Zhichao Shen [1, *], Xidong Zhou [1], Christopher N. Mkono [1], Zhongliang Meng [2, 3], Jakiya Sultana [4], MD Mazedur Rahman [4], Touqeer Aslam [5], Dawood Majeed [6]

[1] School of Marine Science and Engineering, South China University of Technology, Guangzhou, 511442, China
[2] College of Engineering, Qufu Normal University, Rizhao, 276826, China
[3] Institute of Marine Science and Technology, Shandong University, Qingdao, 266237, China
[4] Faculty of Mechanical Engineering and Informatics, University of Miskolc, Miskolc, 3515, Hungary
[5] Shien-Ming Wu School of Intelligent Engineering, South China University of Technology, Guangzhou, 511442, China
[6] Institute of Chemical and Environmental Engineering, Faculty of Chemical and Food Technology, Slovak University of Technology in Bratislava, Radlinskeho 9, 81237 Bratislava, Slovakia
***Corresponding author:** Prof. Zhichao Shen, E-mail address: shenzhichao@scut.edu.cn
[†] Both authors have contributed equally to this study.

Abstract

Small wave energy converters can supply fresh water off the grid only if every link between the sea and the membrane is accounted for. This study couples a time-domain model of the S-shaped buoy SB-1.5 and its ball-screw power take-off (PTO), both experimentally verified in earlier work, with a batch seawater reverse osmosis (RO) model based on solution–diffusion transport, film-theory concentration polarisation, and Pitzer osmotic pressure. The PTO law is anchored to the published bench power and to a mean-to-peak ratio of 0.26 measured from the oscilloscope records, and the buoy follows the Cummins equation calibrated to the published 22 W full-scale absorbed power. In the ShiDao wave climate (2.0 kW/m), the unit absorbs 54.0 W (capture width ratio 1.83%), delivers 19.2 W of electricity and passes 7.3 W of hydraulic power to a 0.6 m² membrane element. With a batch cycle at 30% recovery, this gives about 142 L/day (51.7 m³/yr) at 0.83 g/L, whereas a fixed-pressure once-through module on the same chain gives 10.5 L/day. The hydraulic energy of 1.23 kWh/m³ is about 1.4 times the least work of separation, and the motor–pump set, at 48% stage efficiency, is the weakest link. Monte Carlo and Sobol analyses bound the output at 115–171 L/day (5–95%), with motor–pump efficiency alone explaining 58% of the variance. The simulation is calibrated to published bench tests and full-scale values, and sea trials are the next step. An unconstrained linear damper would absorb 2.6 times more power than the rating-limited PTO, and a 100 W generator raises the annual permeate from 51.7 to 79.6 m³. One unit provides 15 L/day per person for about nine people (volume only, before post-treatment), and eleven units cover a village of one hundred.

Keywords: Wave energy; Power take-off; Ball screw; Batch reverse osmosis; Capture width ratio; Desalination

Nomenclature

A, B	Water and salt permeability of the membrane	m s^{-1} Pa^{-1}, m s^{-1}
A_m	Membrane area	m^2
c, c_b, c_p	Salinity: feed, bulk and permeate (NaCl equivalent)	g L^{-1}
C_d	Viscous drag coefficient of the buoy	–
CWR	Capture width ratio	–
c_g	Group velocity of the waves at the site depth	m s^{-1}
D, R	Buoy diameter and radius	m
d_e	Effective excitation depth	m
d_h, D_s	Hydraulic diameter of the feed channel; diffusivity of salt in water	m; m^2 s^{-1}
E	Concentration polarisation factor, $E = \exp(J/k)$	–
E_h	Hydraulic energy delivered to the membrane in one cycle	J
F_d	Viscous drag force on the buoy	N
F_e, F_{pto}	Wave excitation force and PTO reaction force	N

g, ρ	Gravitational acceleration; water density	m s^{-2}; kg m^{-3}
J	Permeate flux (J_w: wave power per metre of crest, W m^{-1})	m s^{-1}
$K(t)$	Radiation memory kernel	N s m^{-1}
K_h	Hydrostatic stiffness	N m^{-1}
Λ_n	Cycle mean of	$\lvert\sin\theta\rvert^n$
k	Wavenumber; mass-transfer coefficient (Eq. 12)	m^{-1}; m s^{-1}
L, u	Flow-path length of the channel; cross-flow velocity	m; m s^{-1}
M, α_∞	Buoy mass and infinite-frequency added mass	kg
N_φ	Number of generator phases summed (3)	–
n	Exponent of the PTO power law	–
P_{abs}, P_{gen}, P_{el}	Mean absorbed, generator-shaft and electrical power	W
P_{aux}	Auxiliary power (refill and recirculation pumps)	W
P_{dc}, P_{pump}, P_h	Mean power after conditioning, at pump shaft, and hydraulic to the membrane	W
P_{pk}	Peak power of one generator phase	W
P_r	Rated generator shaft power, the product of the limit force and the limit speed	W
Q_p, V_p	Permeate flow rate; permeate volume of one cycle	m^3 s^{-1}; m^3
Re, Sc, Sh	Reynolds, Schmidt and Sherwood numbers	–
r	Final recovery ratio of a batch cycle	–
SEC_h, SEC_{el}	Hydraulic and electrical specific energy consumption	kWh m^{-3}
T, T_p, H_s	Feed temperature; peak period and significant wave height	K; s; m
v, v_{lim}	Screw-nut speed and its limit at 3,000 rpm	m s^{-1}
w_{min}	Least work of separation	kWh m^{-3}
x, x_0	Load fraction of the motor–pump set; part-load constant of the efficiency map	–
z	Heave displacement of the buoy	m
Γ	Excitation force per unit wave amplitude	N m^{-1}
ΔP, ΔP_{ch}	Applied pressure and channel pressure drop	bar
η_c, η_{mp}, η_t	Efficiency of conditioning, motor–pump set and PTO transmission	–
η_r	Rated-load efficiency of the motor–pump set	–
η_{II}	Second-law efficiency of the RO stage	–
λ	Friction factor of the feed channel	–
κ	Ratio of cycle-mean to peak power of one phase (0.26)	–
π, π_f	Osmotic pressure; of the feed	bar
ω, ω_n	Wave frequency and heave natural frequency	rad s^{-1}
Abbreviations	C-HS, cylindrical–hemispherical; PTO, power take-off; RAO, response amplitude operator; RO, reverse osmosis; SB-1.5, S-shaped buoy of 1.5 m diameter; TDS, total dissolved solids; WHO, World Health Organization; SEC, specific energy consumption; CWR, capture width ratio; TDS, total dissolved solids; MTS, Mechanical Test and Sensing system.	

1 Introduction

Water and energy shortages arrive together on small islands, remote coasts and offshore platforms. Diesel generators carry most of the load there, and every litre of fuel has to be shipped in. Waves offer a local resource that is available day and night, and turning it into drinking water is almost as old as wave energy research itself (Folley and Whittaker 2009; Leijon and Boström 2018). Interest has returned in recent years, and heaving and pitching converters were investigated by (Nivetha and Abdul Akbar 2026).

The research base behind this interest is broad and still expanding. A bibliometric survey of 619 Scopus papers from 1979 to 2021 recorded a steady rise in wave-energy output over the last decade, with the United States the most prolific publisher, the United Kingdom leading collaboration and China third with 63 articles (Ola et al. 2026). Resource studies have shifted in a similar direction, away from headline power densities and toward the question of where a converter can operate year-round. Mithun et al. combined thirty years of WAVEWATCH III hindcasts with a consistency metric for the Indian coast and found that onshore sites give up only about 15% of the energy available offshore, which favours the shallow, accessible sites that a small water unit needs (Mithun et al. 2025). Size brings its own trouble. McLeod and Ringwood studied wave-powered data buoys, whose output runs from milliwatts to the kilowatt scale, and pointed out that friction is magnified at small scales and

can affect how well a power take-off (PTO) works (McLeod and Ringwood 2022). A converter that feeds a membrane with a few tens of watts sits in this same demanding range.

Most work on wave-driven desalination follows the hydraulic route. A float or flap pumps seawater directly through a reverse osmosis (RO) membrane, eliminating the electrical stage. Folley and Whittaker estimated the cost of water from an autonomous plant of this kind (Folley and Whittaker 2009). Mi et al. built a scaled system around a piston pump and an accumulator, raised its specific productivity by about 17% through valve tuning, and measured 2.23 m^3/kWh in the tank, which they projected to 0.22 m^3/kWh at full scale with real seawater salinity (Mi et al. 2023). Simmons and Van de Ven compared PTO architectures for wave-powered RO and showed that the architecture shapes both the water output and the scope for co-producing electricity (Simmons and Van de Ven 2023). Other ocean resources have been paired with RO as well. Nakib et al. studied ocean thermal energy conversion, which can drive desalination but operates at efficiencies of only 3 to 5% and is discussed mainly for tropical regions (Nakib et al. 2025).

Waves do not supply a steady pressure, and this is the central difficulty. Sitterley et al. exposed spiral-wound membranes to large feed-pressure fluctuations for about 1,770 h and measured a 7.4% loss of permeability while salt rejection stayed above 99%, so membranes tolerate fluctuation better than once feared (Sitterley et al. 2022). Batch and semi-batch operation changes the picture further. If pressure is allowed to rise as the feed concentrates, the energy per cubic metre falls towards a small multiple of the thermodynamic minimum (Warsinger et al. 2016). Das et al., working on a wave-powered plant with an energy recovery device, reported that conventional operation needs roughly 10 to 36 kWh/m^3 (Das et al. 2024). The thermodynamic floor sets the scale: Elimelech and Phillip put the least work of separating seawater at 50% recovery near 1.06 kWh/m^3 (Elimelech and Phillip 2011). Every real system pays a premium on top of that for finite recovery, driving-pressure margins and pump inefficiency. For a source delivering tens of watts, that premium decides whether the system yields a glass of water or a bucket.

A second route runs through electricity. A mechanical PTO converts the slow heave of a float into rotation, a generator turns it into electrical power, and a conventional motor-driven pump feeds the membrane. This route decouples the sea from the membrane, so storage, power electronics, and a pump not tied to the wave period can all be used. Mechanical PTOs based on motion rectifiers have been tested on the bench and at sea (Liang et al. 2017; Li et al. 2020). The authors have developed a ball-screw PTO with two one-way gears and an optional flywheel, tested together with an S-shaped buoy (Ahmed et al. 2023b), together with bulbous-bottomed resonant buoys (Ahmed et al. 2022), a Wavestar-like array with I-shaped PTOs (Ahmed et al. 2023a) and a Froude-scaled design for floating cities (Ahmed et al. 2025). Wave-flume tests at model scale verified the heave advantage of these buoys, and the heave simulations were checked against published tank data. The bench test campaign of (Ahmed et al. 2023b) also provides the measured PTO power, efficiency and oscilloscope records used in this paper.

Direct mechanical drives show how much the generator decides. Avalos et al. built a wave-to-wire model of a point absorber with a hinged arm and a pulley-driven generator and reported a maximum mean power of about 28 kW and a capture width ratio of up to 36.5% (Avalos et al. 2024). The best results came from the larger of the two generators they tried. When the generator speed passed its rated value, the absorber and the generator uncoupled, and the buoy moved almost freely, so nothing was produced. The speed rating is therefore part of the converter, not an afterthought. Water production adds another layer. Zolghadr et al. tested a paddle-type converter in a laboratory flume to move seawater towards an RO plant (Zolghadr et al. 2024). Output pressure rose with paddle width,

fell as the wave period grew, and was most sensitive to water depth. That device delivers pressure rather than electricity, and it was characterised at model scale.

Two further issues are particular to small units. The first is the power metric. Bench campaigns of mechanical PTOs commonly quote the peak of a rectified voltage envelope. In contrast, the membrane responds to the energy delivered over a cycle, so the ratio between mean and peak power has to be measured and carried through the chain. The second is the behaviour of the membrane and pump at a few watts. At such power, flux is low, salt passage through the membrane rises in proportion, and small pumps run far below their rated point, so energy per cubic metre and permeate salinity depend on how the unit follows the power it receives, not only on the pressure it can reach.

Taken together, these studies leave three gaps. The first is continuity. Hydraulic-route studies start at the pump, and mechanical-PTO studies stop at the generator terminals, so a measured PTO characteristic is rarely followed through the buoy hydrodynamics and a real sea-state climate to litres per day and permeate salinity. Direct-drive batch RO has been modelled (Brodersen et al. 2022), and small-scale RO has run efficiently over a wide range of conditions (Thomson et al. 2003), yet neither starts from a verified wave converter. The second is the generator limit. Work on direct mechanical drives shows that a speed rating can uncouple the converter from its generator (Avalos et al. 2024). Still, the implication of that limit and the generator size for annual water yield have not been quantified. The third is a common yardstick. Wave energy research judges a converter by its capture width ratio, the absorbed power divided by the wave power over one buoy width, while desalination research uses specific energy consumption. One ledger that carries both measures from the sea to the permeate would let the two communities compare designs on the same basis, and it would show at once whether a poor result comes from the converter, the generator, the electronics or the membrane. Such a ledger has rarely been drawn for a verified buoy.

This paper closes these gaps with a coupled simulation that gives equal weight to the wave-energy chain and to the desalination stage. Its contribution is an end-to-end energy ledger for a buoy and PTO with verified inputs, from sea state to permeate, including the correction from peak to mean power and the effect of generator rating. Four objectives follow. First, to show how much of the 2.0 kW/m wave resource reaches the membrane and where it is lost. Second, to estimate the daily and annual permeate volume and its salinity over a year of measured sea states, with the uncertainty of the result. Third, to establish how far the generator rating limits the yield. Fourth, to rank the links of the chain and the RO design levers by what each would gain.

The verified SB-1.5 buoy from (Ahmed et al. 2023b) is modelled in the time domain with the Cummins equation and is excited by the irregular seas of the ShiDao site. The ball-screw PTO enters through its bench-derived force–speed law, including the generator speed rating. The electrical output feeds a conditioning stage, a part-load motor–pump set and a batch RO cycle that follows the available power. The RO model rests on solution–diffusion transport, film-theory concentration polarisation, Schock–Miquel spacer hydraulics and Pitzer osmotic pressure, and it is calibrated to a commercial 2514 element and to the least work of separation. Verification checks, an annual energy balance, a one-week simulation, a Monte Carlo and Sobol uncertainty analysis, and design-lever and generator-rating sweeps complete the study.

Section 2 summarises the verified inputs, Section 3 sets out the models, Section 4 verifies them, Section 5 presents the results, Section 6 discusses them against the literature, and Section 7 concludes.

2 System and verified inputs

Figure 1 outlines the energy chain from the sea state to the permeate, and the verified inputs of its first three blocks are summarised in this section.

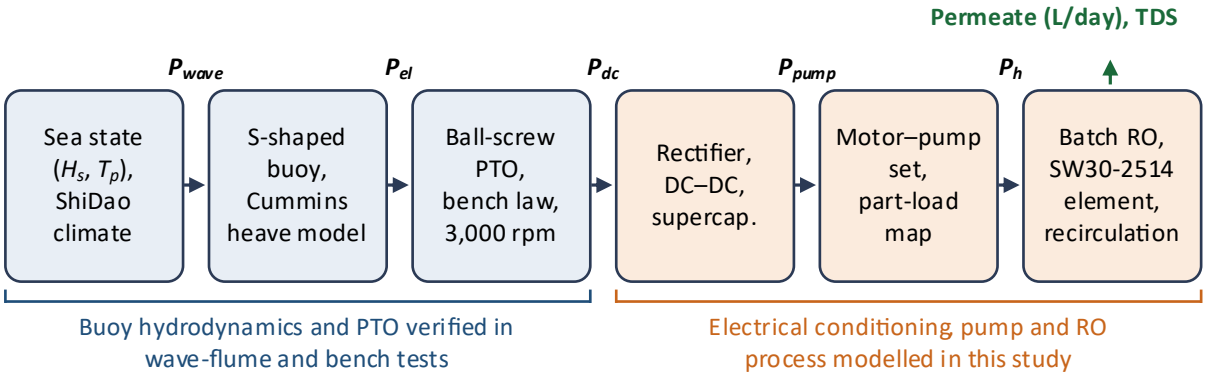


Fig. 1 Energy chain of the wave-driven water unit. The first three blocks (sea state, buoy and PTO) carry verified inputs; the last three (conditioning, motor–pump set and batch RO) are modelled using the parameters in Tables 2 and 3. Power labels between the blocks follow the nomenclature

2.1 Converter and bench results

The converter is the S-shaped buoy SB-1.5, with a diameter of 1.5 m, a draft of 1.46 m, a mass of 3,000 kg and a heave natural frequency of 1.9 rad/s (Ahmed et al. 2022, 2023b). Its heave advantage over the cylindrical–hemispherical (C-HS) reference was established in model-scale wave-flume tests with Froude-scaled 3D-printed models in regular and irregular waves (Ahmed et al. 2025). The simulation tools behind the full-scale predictions were checked against those tests and published tank data, with a response-amplitude error of 8.6% and a power error of 4.3% (Ahmed et al. 2022). The site is ShiDao in the Yellow Sea, with a mean depth of 44 m.

The buoy drives a power take-off consisting of a ball screw with a 64 mm lead, two one-way gears and an 18:1 gear ratio into a three-phase generator rated at 60 W and 3,000 rpm. A bench campaign on an MTS machine, as shown in Figure 2, imposed a sinusoidal stroke with 40 mm amplitude at six frequencies with a 6 Ω load and two frequencies with a 3 Ω load (Ahmed et al. 2023b). Table 1 lists the measured single-phase peak power (P_{pk}). The overall experimental uncertainty was 5.46%, and the measured conversion efficiency reached 52.7% at 0.3 Hz and 71.6% at 0.6 Hz. At 6 Ω, the peak power follows a power law of frequency with an exponent of 1.72 (95% confidence interval 1.45–1.98, R^2 = 0.988), which differs significantly from the viscous value of 2 (t = −2.99, p = 0.040); the 3 Ω pair gives 1.64.

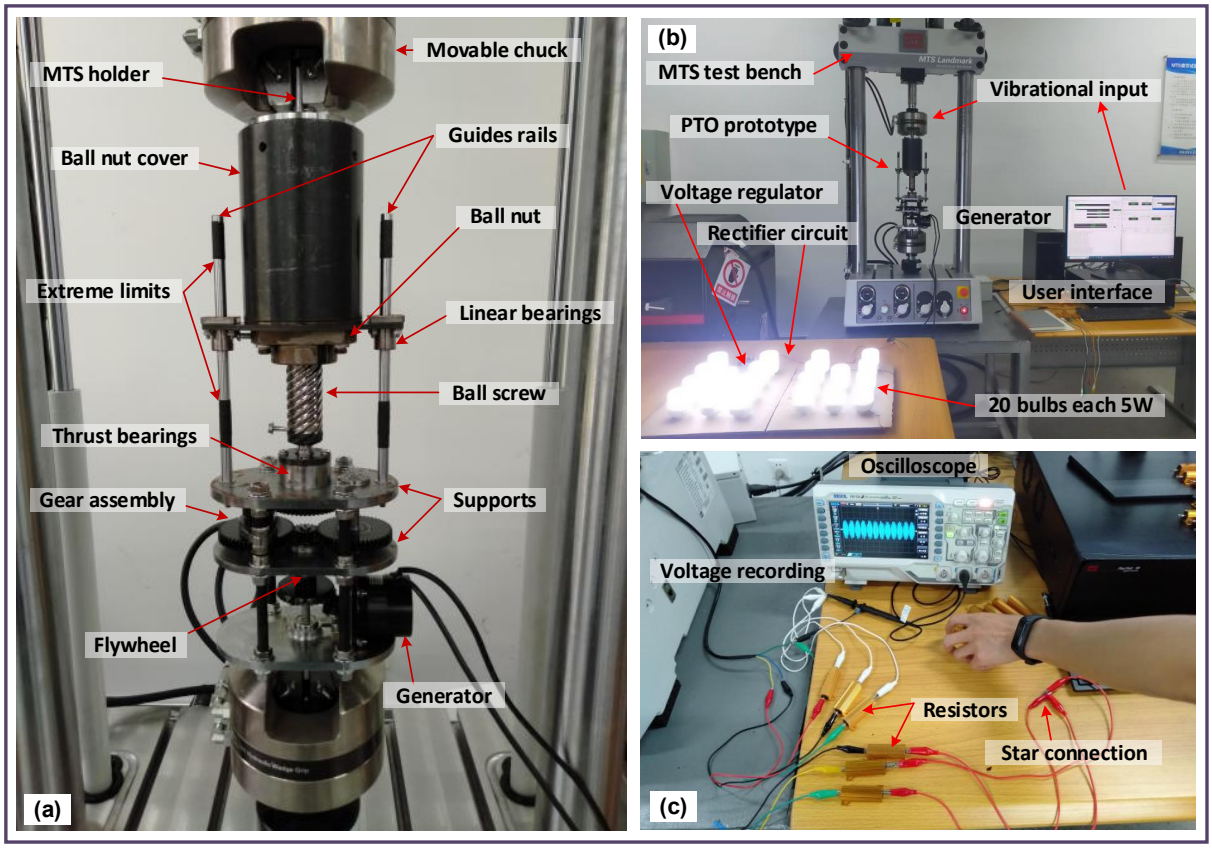


Fig. 2 The power take-off test campaign on the MTS test bench, conducted in the authors' earlier study (Ahmed et al. 2023b) at Yibin Research Institute of Southwest Jiaotong University, Yibin, Sichuan, (image reused with permission of the publisher)

Table 1. Bench inputs of the ball-screw PTO (Ahmed et al. 2023b): single-phase peak power (P_{pk}) at 40 mm amplitude, the three-phase envelope peak, and the cycle-mean electrical power $\bar{P}_{el} = 3\kappa P_{pk}$ with $\kappa = 0.26$. Screw speeds use $v_{pk} = 2\pi f A$.

Load (Ω)	f (Hz)	v_{pk} (m/s)	P_{pk}, one phase (W)	Three-phase envelope peak (W)	$\bar{P}_{el}$ (W)
6	0.1	0.025	0.437	1.31	0.34
6	0.2	0.050	1.07	3.21	0.83
6	0.3	0.075	2.16	6.48	1.68
6	0.4	0.101	4.1	12.30	3.20
6	0.5	0.126	6.16	18.48	4.80
6	0.6	0.151	9.23	27.69	7.20
3	0.3	0.075	4.5	13.50	3.51
3	0.6	0.151	14.0	42.00	10.92

2.2 Mean-to-peak ratio

The tabulated P_{pk} is the maximum of v^2/R_e on one phase, whereas the membrane responds to the mean over a cycle. Because the one-way gears rectify the motion, each phase delivers a lobe of voltage once per half cycle, and the carrier amplitude follows the lobe envelope. The ratio κ of the cycle-mean to the peak power of one phase, Eq. (1), was obtained from the squared voltage envelopes of the four oscilloscope records at 6 Ω and 40 mm (0.3 and 0.6 Hz, with and without the flywheel). The values were 0.258, 0.269, 0.261 and 0.251, with a mean of 0.260 and a standard deviation of 0.008 (Figure 3). The ratio does not depend on frequency or the flywheel, which identifies it as a property of the PTO. The coefficient κ is a shape factor of the rectified voltage envelope; it is normalised by the peak and so does not depend on the load resistance. It is taken from the 6 Ω records, the only oscilloscope data

available. It replaces the constant-amplitude value of 0.5, and the permeate estimates are accordingly about half of what an ideal sinusoid would give.

$$\kappa = \frac{\langle v^2 \rangle}{v_{\max}^2}, \qquad \bar{P}_{\mathrm{el}} = N_{\varphi}\, \kappa\, P_{\mathrm{pk}} \tag{1}$$

The bench power P_{pk} fixes the amplitude and κ fixes the shape, so Eq. (1) with $N_{\varphi} = 3$ gives the cycle-mean electrical power of all three phases. At the 3 Ω condition, this is 3.51 W at 0.3 Hz and 10.9 W at 0.6 Hz (Table 1). The 13.5 W quoted for 0.3 Hz in the abstract of (Ahmed et al. 2023b) is the three-phase envelope peak (3 × 4.5 W), and the cycle-mean value determines the water output.

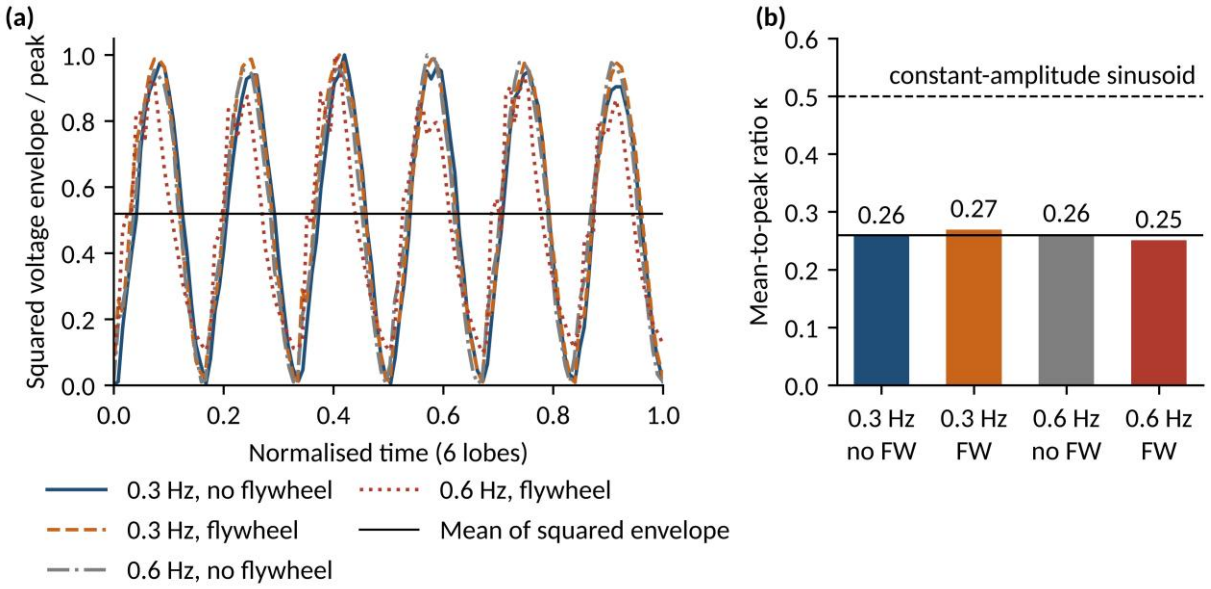


Fig. 3 Mean-to-peak power ratio from the published oscilloscope records (Ahmed et al. 2023b) (6 Ω, 40 mm). (a) Squared voltage envelope normalised by its peak for four traces (FW, flywheel); the solid line marks the mean. (b) κ for each trace; the dashed line is the value of a constant-amplitude sinusoid and the solid line the mean of the four traces

2.3 Site climate

The wave climate is taken from measured wave records at the ShiDao site, which is a Chinese coastal station, with the data source, National Marine Science Data Center (http://mds.nmdis.org.cn/), used in earlier study (Ahmed et al. 2022). The records show a modal cell near $H_{\mathrm{s}} = 0.5$ m and $T_{\mathrm{p}} = 4.5$ s, with 84% of occurrences having T_{p} between 4 and 8 s and a mean wave power of about 2 kW/m (Ahmed et al. 2022, 2023b). The significant wave height follows a lognormal distribution (median 0.658 m, logarithmic standard deviation 0.466) and the peak period, conditional on height, follows a lognormal distribution with median $T_{\mathrm{p}} = 5.04$ s $(H_{\mathrm{s}}/0.5\ \mathrm{m})^{0.372}$ and a logarithmic standard deviation of 0.170. The fitted distribution reproduces the measured statistics, with 11% occurrence in the modal cell, 84% of occurrences with T_{p} between 4 and 8 s and 2.00 kW/m. Sea states are represented by JONSWAP spectra with an energy period of 0.9 T_{p}, discretised on a grid of 20 height bins (0.2 m) and 13 period bins (1 s) that covers 99.95% of the time; the remainder is excluded, and the probabilities are renormalised. Table 2 collects the parameters of the converter, the PTO and the climate.

Table 2. Parameters of the buoy, the PTO, the conditioning stage and the climate. Status: V, verified in earlier work; M, measured site records; C, calibrated to a published value; D, derived; S, specified with the range used in the uncertainty analysis.

Parameter	Value	Status
Buoy diameter, draft, mass	1.5 m, 1.46 m, 3,000 kg	V (Ahmed et al. 2023b)
Heave natural frequency ω_n	1.9 rad/s	V (Ahmed et al. 2023b)
Site depth	44 m	V (Ahmed et al. 2022)
Hydrostatic stiffness K_h; added mass α_∞	17.77 kN/m; 1,950 kg	D
Excitation $\Gamma(\omega_n)$; effective depth d_e	7.14 kN/m; 2.478 m	C (22 W)
Radiation damping at ω_n	181 N s/m	D
Drag coefficient C_d	0.7 (0.4–1.0)	S
Ball-screw lead; gear ratio	64 mm; 18:1	V (Ahmed et al. 2023b)
Generator rating; speed limit v_{lim}	60 W, 3,000 rpm; 0.178 m/s	V (Ahmed et al. 2023b)
PTO power law (3 Ω)	4.5 W at 0.0754 m/s, n = 1.637	V (Ahmed et al. 2023b)
Mean-to-peak ratio κ; phases N_φ	0.26; 3	V (Ahmed et al. 2023b)
Transmission efficiency η_t	0.527 (0.3 Hz) to 0.716 (0.6 Hz)	V (Ahmed et al. 2023b)
Factor c; power plateau; limit force	1.447; 26.5 W; 190 N	D
Conditioning efficiency η_c	0.85 (0.75–0.95)	S
Motor–pump rating; η_r; x_0	20 W; 0.50 (0.35–0.65); 0.15	S
Climate: H_s median, σ; T_p median, σ	0.658 m, 0.466; 5.04 s, 0.170	M (Ahmed et al. 2022)
Mean wave power; wave power over D	2.00 kW/m; 2,961 W	D

3 Models

3.1 Buoy hydrodynamics

Heave motion z follows the Cummins equation, Eq. (2), in which F_e is the wave excitation force, K_h the hydrostatic stiffness, $K(t)$ the radiation memory kernel, F_{pto} the PTO reaction force and F_d the viscous drag (Cummins 1962; Falnes and Kurniawan 2020). The kernel follows from the radiation damping $B(\omega)$ by Eq. (3), and the Haskind relation expresses $B(\omega)$ through the excitation force per unit amplitude Γ, Eq. (4), where c_g is the group velocity at the 44 m site depth. The added mass $\alpha(\omega)$ follows from the kernel by the Kramers–Kronig relation, and its infinite-frequency value α_∞ is fixed by matching α at ω_n to the heave resonance. The excitation is written as $\Gamma = K_h \exp(-kd_e)$ with an effective depth (d_e) that carries the buoy geometry. Its value, 2.478 m, was calibrated once to the 22 W full-scale absorbed power published for 0.3 Hz (Ahmed et al. 2023b) and was not changed afterwards. The viscous drag, Eq. (5), uses C_d = 0.7. The model gives α_∞ = 1,950 kg, a radiation damping of 181 N s/m and Γ = 7.14 kN/m at ω_n.

$$(M + \alpha_\infty)\ddot{z} = F_e - K_h\, z - \int_0^t K\,(t-\tau)\,\dot{z}(\tau)\,\mathrm{d}\tau - F_{pto} - F_d \tag{2}$$

$$K(t) = \frac{2}{\pi}\int_0^\infty B\,(\omega)\cos(\omega t)\,\mathrm{d}\omega \tag{3}$$

$$B(\omega) = \frac{k\,\Gamma^2}{4\rho g\, c_g}, \qquad \Gamma = K_h exp(-k\, d_e) \tag{4}$$

$$F_d = \frac{1}{2}\,\rho\, C_d\, \pi R^2\, |\dot{z}|\dot{z} \tag{5}$$

3.2 PTO law and speed limit

The PTO is represented by the bench law of (Ahmed et al. 2023b). The single-phase peak power follows Eq. (6), anchored to the 3 Ω points of Table 1 with P_0 = 4.5 W at v_0 = 0.0754 m/s and an

exponent n = 1.637 obtained from the two 3 Ω points. The 3 Ω condition is the higher-power load at which the generator approaches its rating. The 6 Ω exponent of 1.72 changes the annual permeate by +7% (Table 8) and changes no conclusion. The instantaneous three-phase electrical power is given by Eq. (7). The factor c is set so that the cycle mean of a sinusoidal speed reproduces Eq. (1); with $\Lambda_n = \langle|\sin\theta|^n\rangle$ = 0.539, it equals 1.447. The generator rating limits the screw-nut speed to v_{lim} = 3,000 rpm × 64 mm / 18 = 0.178 m/s. Above v_{lim}, a torque limiter holds the force and the electrical power at their rated values (190 N and 26.5 W), and the excess absorbed energy is dissipated in the limiter. The limit force of 190.4 N is not a separate input; it follows from Eqs. (6)–(8) at v_{lim}. It represents the generator operating limit at 3,000 rpm, and the torque limiter is a modelling assumption for it. The 60 W nameplate is the generator maximum; on the 3 Ω load line the generator delivers 26.5 W electrical (33.8 W at the shaft) at 3,000 rpm, an extrapolation of 18% beyond the highest bench speed (0.151 m/s).

$$P_{\mathrm{pk}}(v) = P_0 \left(\frac{|v|}{v_0}\right)^n \tag{6}$$

$$P_{\mathrm{el}}(t) = c\, P_{\mathrm{pk}}\big(\min(|v|, v_{\mathrm{lim}})\big), \qquad c = \frac{N_\varphi\, \kappa}{\Lambda_n} \tag{7}$$

Eq. (7) gives the three-phase power in a form that preserves the cycle mean of Eq. (1). Its instantaneous peak (6.5 W at 0.3 Hz, 3 Ω) is not the three-phase envelope peak of Table 1 (13.5 W = $3P_{\mathrm{pk}}$). The ratio of mean to envelope peak is κ (3.51/13.5 = 0.26). The reaction force on the buoy follows from the generator-shaft power, Eq. (8), with a transmission efficiency (η_{t}) interpolated linearly in speed between the measured 0.527 at 0.3 Hz and 0.716 at 0.6 Hz, and held between 0.30 and 0.80. The force is the instantaneous value at the peak screw speed: 164 N at 0.3 Hz (1.447 × 4.5 W / (0.527 × 0.0754 m/s)), 188 N at 0.6 Hz and 190 N at the limit. Because $P_{\mathrm{pk}} \propto |v|^{1.637}$, the force scales as $|v|^{0.637}$ and tends to zero with the speed, so Eq. (8) has no singularity at v = 0. Figure 4 shows the PTO law and its behaviour in a sea state.

$$F_{\mathrm{pto}} = \mathrm{sgn}(\dot{z})\, \frac{P_{\mathrm{el}}}{\eta_{\mathrm{t}}|\dot{z}|} \tag{8}$$

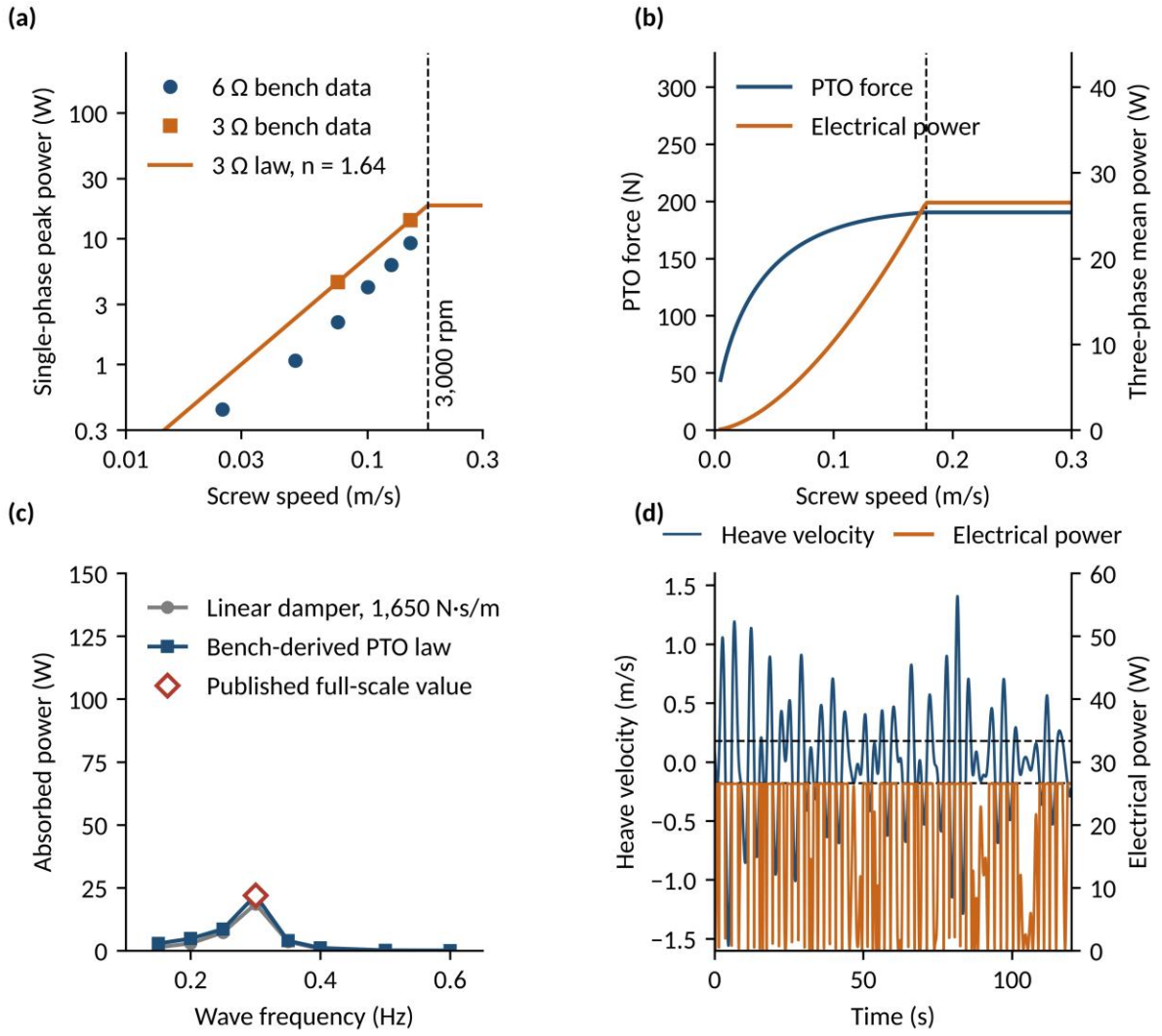


Fig. 4 PTO law and buoy response. (a) Single-phase peak power against screw speed, with the 6 Ω and 3 Ω bench data, the 3 Ω power law and the 3,000 rpm limit. (b) PTO force and three-phase mean electrical power against screw speed. (c) Absorbed power in regular waves for the bench-derived law and for a linear damper, with the published 22 W full-scale value (Ahmed et al. 2023b). (d) Heave velocity and electrical power in a sample sea state (H_s = 0.9 m, T_p = 5.5 s); the dashed lines mark $\pm v_{lim}$

3.3 Conditioning and motor–pump set

The electrical output passes through a rectifier, a DC–DC converter and a supercapacitor buffer with a lumped efficiency η_c = 0.85. The auxiliary loads of the batch cycle, the refill pump (0.3 bar head, efficiency 0.30) and the recirculation pump (efficiency 0.35), are supplied from the conditioned power. The remainder drives a motor–pump set rated at 20 W, Eq. (9). The set follows a part-load map $\eta_{mp} = \eta_r\, x\, (1 + x_0) / (x + x_0)$, with a rated-load efficiency η_r = 0.50. Brodersen et al. assumed 0.85 for a high-pressure pump and 0.65 for a circulation pump in their direct-drive model (Brodersen et al. 2022); because motors and pumps lose efficiency as their size falls, a 20 W set was assigned a lower value, and η_r was varied from 0.35 to 0.65 in the uncertainty analysis. Finally, x is the load fraction and x_0 = 0.15, which reflects the fall in efficiency of small motors and plunger pumps at partial load.

$$P_{dc} = \eta_c P_{el}, \qquad P_{pump} = P_{dc} - P_{aux}, \qquad P_h = \eta_{mp} P_{pump} \tag{9}$$

3.4 Batch reverse osmosis

The RO stage is a closed-loop batch cycle on a spiral-wound 2514 element (Table 3). Permeate flux follows the solution–diffusion model (Eq. 10), where A is the water permeability, ΔP_{ch} is the channel pressure drop, and π_m and π_p are the osmotic pressures at the membrane wall and in the permeate (Wijmans and Baker 1995). Osmotic pressures are computed for a NaCl-equivalent solution with the Pitzer osmotic coefficient (Pitzer and Mayorga 1993), which gives 26.7 bar at 35 g/L and 290 K. Concentration polarisation follows film theory, Eq. (11), with $E = \exp(J/k)$ and the permeate salinity (c_p) fixed by the salt permeability (B). The mass-transfer coefficient and the channel pressure drop use the Schock–Miquel correlations for the feed spacer, Eqs. (12) and (13) (Schock and Miquel 1987). Permeability and salt permeability scale with temperature by $\exp[2{,}640(1/298.15 - 1/T)]$. A and B were calibrated to the manufacturer's test point (32 g/L NaCl, 55 bar, 25 °C, 0.6 m³/d, 99.4% rejection), giving $A = 1.526$ L m^{-2} h^{-1} bar^{-1} and $B = 6.34 \times 10^{-8}$ m/s at 25 °C. A and B were calibrated at 25 °C (298.15 K) and corrected to the operating temperature by the factor in Table 3. The annual simulations use a constant feed of 290 K (16.9 °C), varied from 283 to 297 K in the uncertainty analysis. The least-work check of Section 4 is made at 25 °C and the annual balance at 290 K. A follows from the rated flow and B from the rejection at the test point, so each is fixed by one datum. The area of 0.6 m² is the active area of the 2514 element.

$$J = A\left[\Delta P - \frac{\Delta P_{\mathrm{ch}}}{2} - \left(\pi_{\mathrm{m}} - \pi_{\mathrm{p}}\right)\right] \tag{10}$$

$$c_p = c_b \, \frac{B\,E}{J + B\,E} \tag{11}$$

$$Sh = 0.065\, Re^{0.875}\, Sc^{0.25}, \qquad k = \frac{Sh\, D_s}{d_h} \tag{12}$$

$$\lambda = 6.23\, Re^{-0.3}, \qquad \Delta P_{ch} = \frac{\lambda\, \rho\, u^2 L}{2\, d_h} \tag{13}$$

The hydraulic power (P_h) reaching the membrane is held constant during a cycle, so the applied pressure rises as the brine concentrates and as the flux falls, Eq. (14). The cycle ends at the recovery (r), when a refill with fresh feed starts the next one. The recirculation flow is 4 L/min in a loop of 4 L. The hydraulic energy of a cycle gives the specific consumption, and the least work of separation provides the thermodynamic reference, Eq. (15). The ratio of the two is the second-law efficiency of the RO stage. Within a cycle, P_h is held at the sea-state mean. This is acceptable because the supercapacitor buffer smooths the 3–10 s wave fluctuation over a 12–22 min cycle, and the week simulation (Section 5.5) lets the power change from hour to hour.

$$\Delta P(t) = \frac{P_{\mathrm{h}}}{Q_{\mathrm{p}}(t)}, \qquad Q_{\mathrm{p}} = J\, A_{\mathrm{m}}, \qquad E_{\mathrm{h}} = \int \Delta P\, Q_{\mathrm{p}}\, \mathrm{d}t \tag{14}$$

$$SEC_h = \frac{E_h}{V_p}, \qquad w_{min} = \frac{\pi_f\, ln[1/(1-r)]}{r}, \qquad \eta_{II} = \frac{w_{min}}{SEC_h} \tag{15}$$

Table 3. Parameters of the batch RO model and of the 2514 spiral-wound element.

Parameter	Value
Membrane area; leaf length; channel width	0.6 m²; 0.30 m; 1.0 m
Spacer height; porosity; hydraulic diameter	0.711 mm; 0.89; 0.879 mm
Water permeability A (at 25 °C; at 290 K)	1.526; 1.19 L m^{-2} h^{-1} bar^{-1}
Salt permeability B (at 25 °C; at 290 K)	6.34×10^{-8}; 4.94×10^{-8} m/s
Feed salinity; temperature	35 g/L; 290 K
Feed osmotic pressure π_f	26.7 bar
Recovery (r); loop volume; recirculation flow	0.3 (0.5); 4 L; 4 L/min
Refill head and efficiency; recirculation efficiency	0.3 bar, 0.30; 0.35
Temperature factor	exp[2,640 (1/298.15 − 1/T)]

3.5 Energy balance and metrics

For each sea state, the time-domain model yields the mean absorbed power P_{abs}, the generator-shaft input P_{gen}, the electrical output P_{el} and the fraction of time at the speed limit. The capture width ratio, as used for wave energy converters, relates absorbed power to the wave power over one buoy width, Eq. (16), where J_w is the wave power per metre of crest. CWR uses the absorbed power; whereas the electrical value is stated as such. Annual means are probability-weighted sums over the sea-state matrix. The RO stage is evaluated from a pre-computed table of cycle metrics as a function of hydraulic power, salinity and temperature, so that the annual permeate follows from the distribution of P_h.

$$\mathrm{CWR} = \frac{P}{J_w D} \tag{16}$$

3.6 Numerics and uncertainty

The Cummins equation was integrated with an explicit scheme at a step of 0.05 s and an 18 s memory window. Each of the 150 sea states with non-negligible probability (of the 260 cells of the matrix) was run for 1,500 s with 250 s of start-up and 140 jittered spectral components. Uncertainty was propagated through a quadratic surrogate of the electrical power per sea state, fitted to a 13-point Box–Behnken design over the buoy excitation scale (normal, standard deviation 8.6%, the response error of (Ahmed et al. 2022)), drag coefficient (triangular, 0.4–0.7–1.0) and PTO bench power (normal, 5.46%). Further inputs were the climate scale (0.9–1.0–1.1), η_c (0.75–0.85–0.95), η_r (0.35–0.50–0.65), salinity (30–35–38 g/L) and temperature (283–290–297 K). A scrambled Sobol sequence of 8,192 points gave the output distribution, and first-order and total Sobol indices came from the Saltelli design with the Jansen estimator, 1,024 base samples and eight replicates (Saltelli et al. 2010). The simulation code was developed with the help of a large language model (Claude, Anthropic). The authors reviewed the code, tested it against the analytic and published checks of Section 4, and are responsible for it and for all results.

4 Verification and calibration

Table 4 lists the verification checks. The time-domain code reproduces the analytic heave response of the linear system to 0.6% in velocity and 1.6% in absorbed power. The excitation calibration reproduces the published full-scale value of 22 W. The mean electrical power at the bench condition follows from the PTO law to the digit of Table 1, and the generator-shaft power at 0.3 Hz is consistent with the measured efficiency of 52.7%. The RO model gives a least work of 1.056 kWh/m³ for 35 g/L, 25 °C and 50% recovery compared with 1.06 kWh/m³ in (Elimelech and Phillip 2011), and the element reproduces the manufacturer's test point. Forty synthetic years of hourly sea states give a mean annual permeate within 1% of the probability-weighted expectation. A bounding case in which

the excitation is raised to the hydrostatic limit ($d_e = 0$) increases the annual yield by 17%, which shows how much the calibration depends on the single published power value. Rows marked calibration fix a parameter and are not independent validation. The buoy is therefore calibrated to one published full-scale value and checked against model-scale tests (response amplitude 8.6%, power 4.3%; (Ahmed et al. 2022)), with the excitation scale included in the uncertainty analysis. The batch model conserves salt to 0.01% over a cycle, and the end-of-cycle pressure peaks at 53 bar (59 bar at 38 g/L and 283 K).

Table 4. Verification checks of the coupled model.

Check	Reference	Model	Deviation
Heave velocity, linear damper, regular wave	0.1577 m/s (analytic)	0.1568 m/s	0.6%
Absorbed power, same case	20.51 W (analytic)	20.19 W	1.6%
Absorbed power, 0.3 Hz, full scale	22 W (Ahmed et al. 2023b)	22.0 W	calibration
Mean electrical power, 3 Ω, 0.3 Hz	3.51 W (Table 1)	3.51 W	< 0.1%
Generator-shaft power, 0.3 Hz bench	6.66 W ($\eta_t = 0.527$)	6.66 W	< 0.1%
Least work, 35 g/L, 25 °C, $r = 0.5$	1.06 kWh/m³ (Elimelech and Phillip 2011)	1.056 kWh/m³	0.4%
Element test point (55 bar, 32 g/L)	99.4% rejection, 0.6 m³/d	reproduced	calibration
Annual permeate, 40 synthetic years	51.7 m³ (expectation)	51.2 m³ (SD 0.6)	1.0%
Excitation upper bound ($d_e = 0$)	51.7 m³ (central)	60.7 m³	+17%

5 Results

5.1 Response to sea states

Figure 5 maps the response over the climate matrix. The mean electrical power rises quickly with wave height and reaches the 26.5 W rating plateau in the larger sea states (Fig. 5b). In the modal cell ($H_s = 0.5$ m, $T_p = 4.5$ s) the buoy absorbs 51 W, the generator delivers 19.5 W, and the screw sits at its speed limit for 59% of the time (Fig. 5c). The electrical power exceeds 5 W in 99.5% of the time, 10 W in 98.9% and 20 W in 45%. As a result, sea states with $H_s \leq 1$ m provide 79% of the annual electrical energy and those above 2 m only 0.9%. Sea states above 3 m (0.05% of the time) are treated as survival mode with zero output.

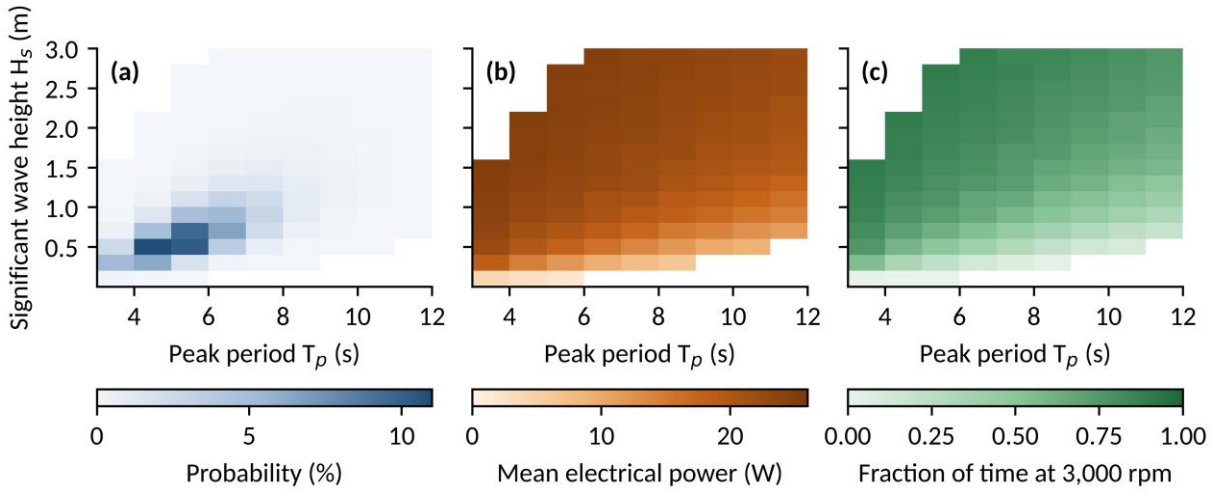


Fig. 5 Response over the climate matrix. (a) Probability of occurrence. (b) Mean electrical power. (c) Fraction of time at the 3,000 rpm speed limit

5.2 Batch RO under power-following

Figure 6a shows one cycle at the annual mean hydraulic power of 7.27 W. At $r = 0.3$, the cycle lasts 12.1 min, the pressure ramps from 39.7 to 49.6 bar, and the flux falls from 11.0 to 8.8 L m^{-2} h^{-1}. At $r =$ 0.5, the cycle lasts 22.4 min, and the pressure reaches 63.6 bar. The hydraulic specific energy depends

on the unit power (Fig. 6b). At r = 0.3, it rises from 0.79 kWh/m³ at 0.5 W to 1.75 kWh/m³ at 25 W because a higher flux requires a larger pressure above the osmotic pressure. The permeate salinity moves the other way (Fig. 6c). It falls from 5.9 g/L at 0.5 W to 0.41 g/L at 25 W, since the low flux at low power makes salt passage dominate. The mean permeate salinity drops below 1 g/L at about 6 W for r = 0.3 and at about 10 W for r = 0.5, and below 0.5 g/L at about 16 W for r = 0.3. The annual mean of 7.3 W therefore places the unit in the range where the cycle gives a low-salinity permeate at modest energy.

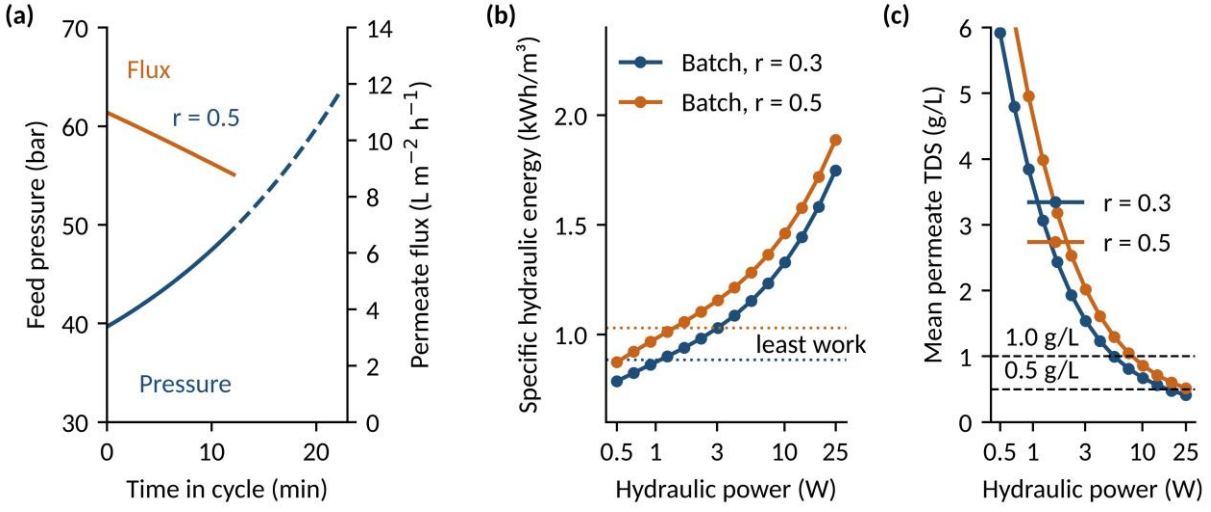


Fig. 6 Batch RO cycles under power-following. (a) Feed pressure and permeate flux during one cycle at the annual mean hydraulic power of 7.27 W. (b) Specific hydraulic energy against hydraulic power; the dotted lines show the least work. (c) Mean permeate salinity against hydraulic power; the dashed lines mark 0.5 and 1.0 g/L

5.3 Annual energy balance

Table 5 and Fig. 7 give the stage-by-stage balance for the annual climate. The wave power over the buoy width is 2,961 W, and the buoy absorbs 54.0 W, a capture width ratio of 1.83%. The torque limiter dissipates more than half of the absorbed energy; the generator shaft receives 25.6 W, a 47% stage transfer. The generator delivers 19.2 W of electricity (75%) with a capacity factor of 0.72 against the 26.5 W plateau; the conditioning stage passes 16.3 W (85%), the auxiliaries take 1.2 W, and 15.1 W reaches the pump shaft. The motor–pump set converts this to 7.3 W of hydraulic power at a mean efficiency of 48%, making it the lowest-efficiency stage after the speed limiter. The RO process then holds a second-law efficiency of 0.72 at r = 0.3, and the minimum separation work corresponds to 5.2 W. Overall, 0.25% of the incident wave power reaches the membrane as hydraulic power and 0.18% ends up as separation work. The 48.8 W lost between the 54.05 W absorbed and the 5.21 W of separation work divides into 28.5 W in the limiter, 6.4 W in the transmission, 2.9 W in conditioning, 1.2 W in the auxiliaries, 7.9 W in the motor–pump set and 2.1 W of RO irreversibility.

Table 5. Annual stage-by-stage energy balance of one unit (mean powers in W, electrical and volumetric figures per unit). SEC_h is counted at the membrane and SEC_{el} at the generator terminals.

Quantity	Batch r = 0.3	Batch r = 0.5
Wave power over buoy width	2,961	2,961
Absorbed by PTO force (CWR 1.83%)	54.0	54.0
Generator-shaft input	25.6	25.6
Electrical output (CWR 0.65%)	19.2	19.2
After conditioning	16.3	16.3
Auxiliaries (refill, recirculation)	1.16	0.92
Pump shaft input	15.1	15.4
Hydraulic power to the membrane	7.27	7.40
Least work of separation	5.21	5.57
Motor–pump efficiency (mean)	0.48	0.48
Second-law efficiency of the RO stage	0.72	0.75
SEC_h (kWh/m³); least work (kWh/m³)	1.23; 0.88	1.37; 1.03
SEC_{el} at generator terminals (kWh/m³)	3.24	3.54
Permeate (L/day; m³/yr)	141.7; 51.7	129.9; 47.4
Mean permeate salinity (g/L)	0.83	1.06

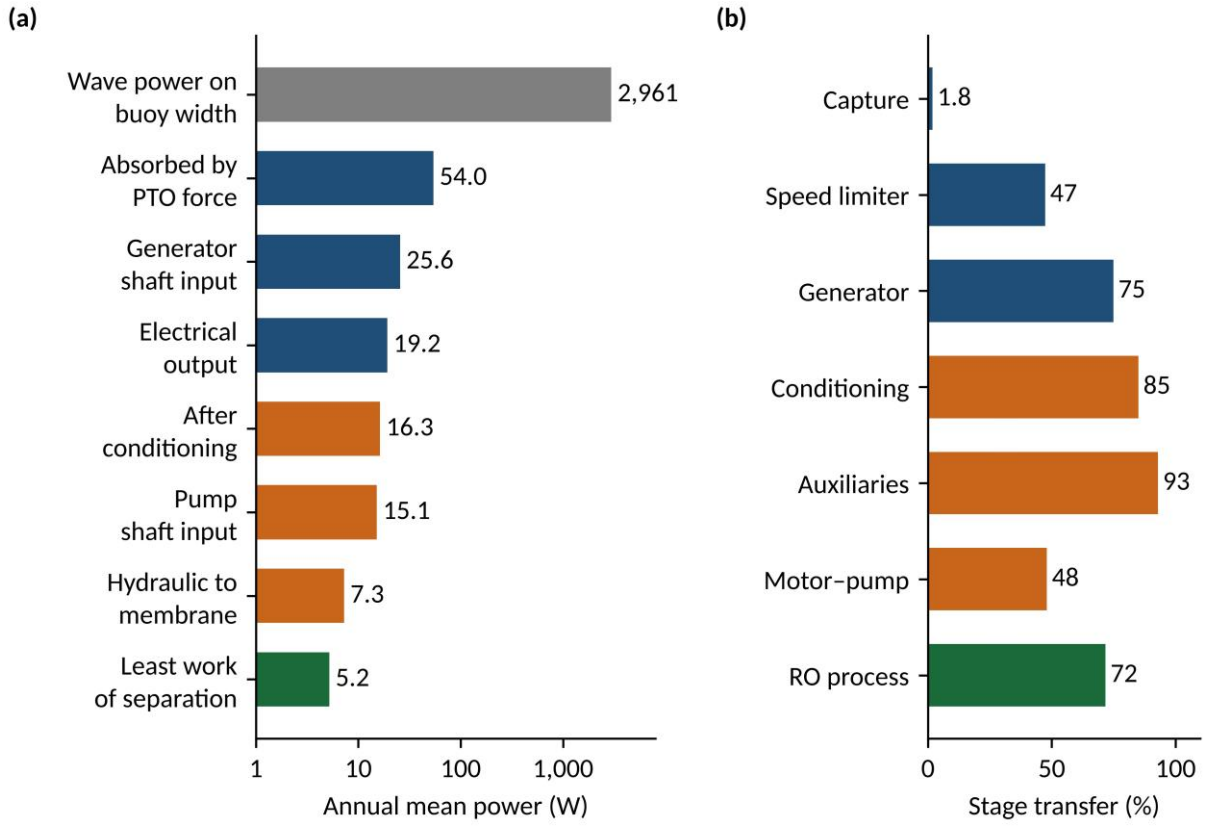


Fig. 7 Annual energy balance at r = 0.3. (a) Mean power at each stage on a logarithmic axis. (b) Transfer efficiency of each stage

5.4 Annual yield and water quality

Table 6 compares the operating modes over the annual climate. The batch cycle at r = 0.3 yields 141.7 L/day (51.7 m³ per year) with a mean permeate salinity of 0.83 g/L and a hydraulic specific energy of 1.23 kWh/m³, which is about 1.4 times the least work of 0.88 kWh/m³. The electrical specific energy, counted at the generator terminals, is 3.24 kWh/m³. Raising the recovery to 0.5 lowers the yield by 8% to 129.9 L/day, raises the specific energy to 1.37 kWh/m³ and lifts the salinity to 1.06 g/L. A fixed-

pressure once-through module at 60 bar and 10% recovery, fed by the same chain, yields only 10.5 L/day at 9.5 g/L, so the batch cycle delivers 13.5 times more water, and a low-salinity permeate. The WHO taste ranking places 0.83 g/L in the fair band (600–900 mg/L) and 1.06 g/L in the poor band (900–1,200 mg/L) (Cotruvo 2017).

The buoy shape matters, but less than the cycle. Replacing the S-shaped buoy with the C-HS buoy lowers the absorbed power by 11% (48.2 against 54.0 W) and the annual yield by 4.3% (135.7 against 141.7 L/day), because the PTO is saturated for 58% of the time and compresses the difference. Forty synthetic years of hourly sea states give an annual permeate of 51.2 ± 0.6 m³ (range 49.6–52.4 m³), so the interannual variation is only 1.2%. The synthetic years use hourly sea states with a first-order autoregressive model of 36 h correlation time, which keeps storm persistence. The 1.2% is the sampling variability of a stationary climate, not the long-term uncertainty of the resource.

Table 6. Annual yield per unit by operating mode and buoy. S1: fixed 60 bar, once-through, $r = 0.1$; S2 and S3: batch cycles at $r = 0.3$ and 0.5. The band is the 5–95% interval of the Monte Carlo analysis. SEC_h is counted at the membrane and SEC_{el} at the generator terminals.

Scenario	L/day	m³/yr	5–95% (L/day)	Salinity (g/L)	SEC_h (kWh/m³)
S1 fixed pressure, once-through	10.5	3.82	—	9.5	16.7
S2 batch, $r = 0.3$	141.7	51.7	115–171	0.83	1.23
S3 batch, $r = 0.5$	129.9	47.4	105–158	1.06	1.37
S2 with C-HS buoy	135.7	49.5	—	—	—
S2, excitation upper bound	166.3	60.7	—	—	—

5.5 One-week simulation

Figure 8 follows the unit through a synthetic week of hourly sea states in a stateful simulation with the batch cycle running continuously. Wave height stays between 0.4 and 1.1 m for the first five days and then rises to 3.7 m in a storm. The electrical output stays between 17.5 and 23.5 W and the hydraulic power between 6.5 and 9.2 W, while the unit runs. The feed pressure ramps and resets about every 12 min within 39–52 bar. The unit completes 875 cycles and produces 1,051 L at 0.77 g/L. Only the five hours above 3 m interrupt production.

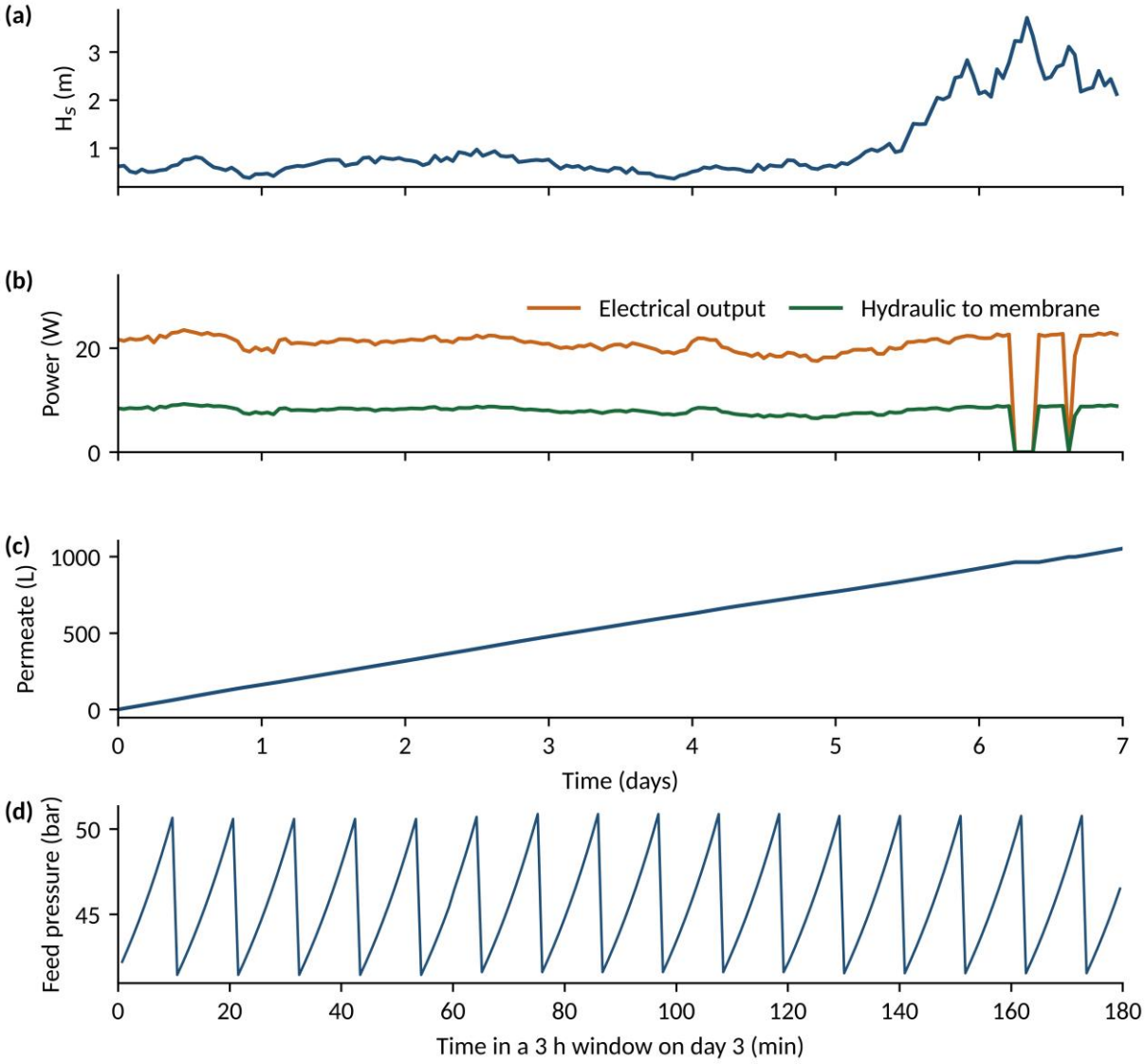


Fig. 8 One-week simulation with the batch cycle running continuously. (a) Significant wave height. (b) Electrical output and hydraulic power to the membrane. (c) Cumulative permeate. (d) Feed pressure in a 3 h window on day 3

5.6 Uncertainty

The Monte Carlo analysis gives a mean annual permeate of 52.0 m³ with a standard deviation of 6.2 m³ at $r = 0.3$, and a 5–95% band of 42.0–62.5 m³ (115–171 L/day), as shown in Fig. 9a. The mean of 52.0 m³ differs from the nominal 51.7 m³ because the output is a nonlinear function of the inputs. At $r = 0.5$ the mean is 47.7 m³ and the band 38.3–57.7 m³ (105–158 L/day). The permeate salinity at $r = 0.3$ lies between 0.66 and 1.03 g/L (5–95%). The Sobol indices of Fig. 9b are dominated by one input: the motor–pump efficiency explains 58% of the variance. The conditioning efficiency follows with 14%, the PTO bench power with 13%, the salinity with 6% and the buoy excitation with 6%. Temperature contributes 2%, and the wave climate and the drag coefficient contribute less than 1% each. First-order and total indices coincide to within 0.003, so the output is nearly additive in its inputs.

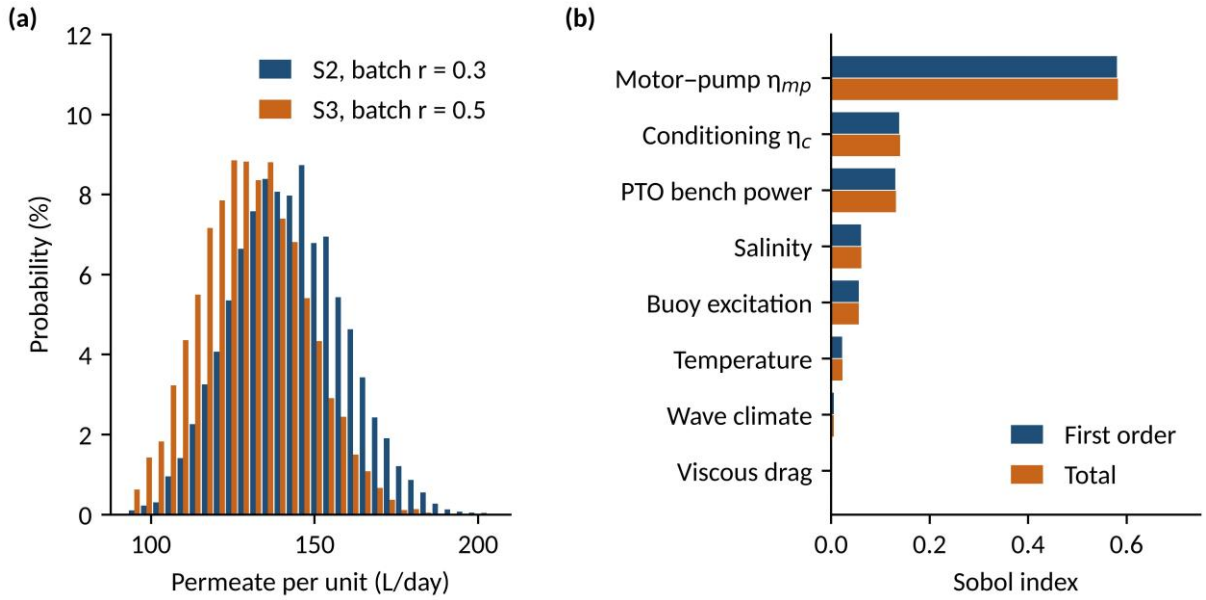


Fig. 9 Annual uncertainty. (a) Distribution of the annual permeate of one unit, in L/day, for batch cycles at r = 0.3 (S2) and r = 0.5 (S3). (b) First-order and total Sobol indices at r = 0.3

5.7 Design levers

Figure 10 shows three levers of the RO stage. Raising the recovery from 0.2 to 0.6 increases the hydraulic specific energy from 1.17 to 1.45 kWh/m³ (+23%). Salinity increases from 0.75 to 1.28 g/L, and the model remains 0.32–0.35 kWh/m³ above the least work across all recoveries (Fig. 10a). A larger membrane lowers specific energy but increases salt passage, because flux falls. At 0.6 m², the salinity is 0.83 g/L; at 1.2 m², the energy falls to 1.10 kWh/m³, and the salinity rises to 1.37 g/L. A smaller membrane of 0.3 m² gives 0.50 g/L at the cost of 15% more energy (1.40 kWh/m³) (Fig. 10b). The recirculation flow has an optimum at 3–4 L/min, where the electrical energy is 3.12 kWh/m³; at 1 L/min the polarisation raises it to 3.51 kWh/m³ and at 8 L/min the pumping power raises it to 3.66 kWh/m³ (Fig. 10c).

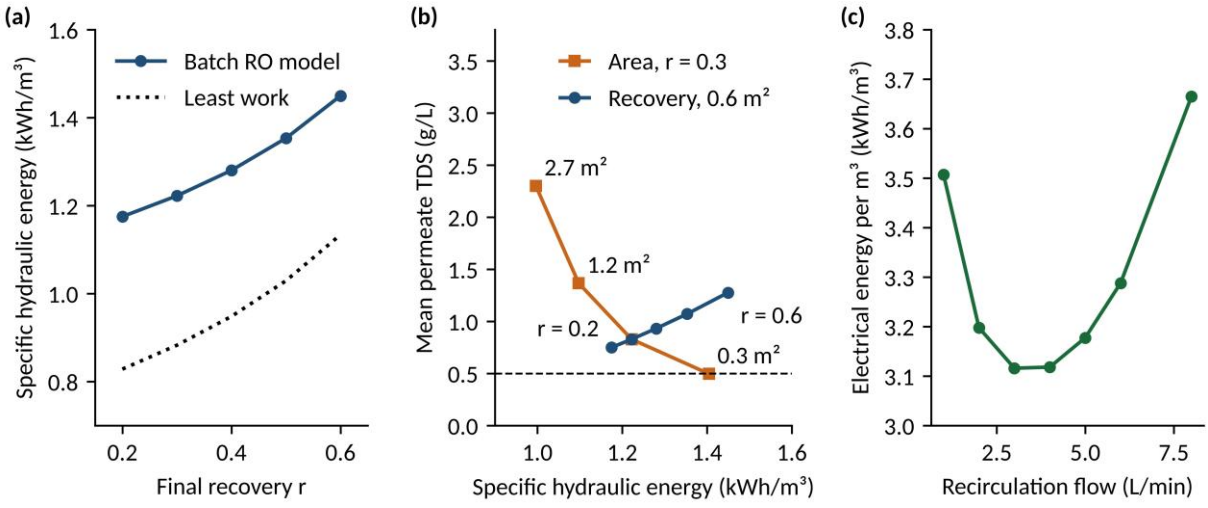


Fig. 10 Design levers. (a) Hydraulic specific energy against recovery, with the least work. (b) Mean permeate salinity against specific energy for the recovery sweep at 0.6 m² and the area sweep at r = 0.3; the dashed line marks 0.5 g/L. (c) Electrical energy per cubic metre against recirculation flow

5.8 Generator rating and speed limit

The as-built generator limits the shaft power to 33.8 W (the nameplate rating is 60 W), the product of the 190.4 N limit force and the 0.178 m/s limit speed, and the buoy exceeds that speed for 58% of the time. To quantify this limit, we raised the screw-speed limit to the torque already exercised on the bench, so that the PTO law is unchanged below 0.178 m/s and the force stays at 190.4 N above it. The shaft-power rating $P_r = 190.4\ \text{N} \times v_{lim}$ then takes the values 60, 80, 100 and 150 W. The motor–pump rating scales with the electrical plateau (20 W as built and 36.2, 48.3, 60.3 and 90.5 W), the transmission efficiency is capped at 0.80, and the batch-RO table is extended to 123 W of hydraulic power. All other inputs are those of Sections 2 and 3 (Tables 2 and 3), and the sea-state matrix is simulated again for each rating; the as-built case reproduces Table 6. Raising the generator rating alone leaves the yield unchanged, because the 0.178 m/s speed limit binds first. The sweep is therefore a system-redesign scenario in which the speed limit, generator and motor–pump rating are raised together, and it assumes the screw, gears and bearings can run at the higher speed.

Table 7 and Fig. 11 give the results. Because the force law is the same, the buoy absorbs 54.0 W at every rating, and the rating decides how much of it is delivered. The annual electrical output rises from 19.2 W to 29.1 W at 60 W (+52%) and to 36.9 W at 100 W, and the annual permeate rises from 51.7 m³ to 69.8 m³ (+35%) and 79.6 m³ (+54%). The return then falls quickly. From 100 W to 150 W, output gains 3.8 W and the permeate only 1.1%, because the sea states that drive the screw faster than 0.525 m/s are rare, and the limiter is active for 16% of the time at 100 W and 5% at 150 W. The permeate salinity improves from 0.83 to 0.58 g/L. The electrical specific energy rises from 3.24 to 4.06 kWh/m³ at 100 W because the added energy arrives in energy-rich sea states and is processed at up to 71 bar. A 100 W generator, 1.9 times the mean absorbed power, therefore delivers 99% of the yield of the 150 W unit and raises the as-built yield by a factor of 1.5.

Table 7. Annual energy balance and permeate for five generator ratings (recovery 0.3). Share is the electrical output as a percentage of the 54.0 W absorbed. *As built.

Rating (W)	Speed limit (m/s)	Shaft (W)	Elec. (W)	Share (%)	Hyd. (W)	L/day	m³/yr	TDS (g/L)	SEC_{el}
33.8*	0.178	25.6	19.2	35.5	7.3	141.7	51.7	0.83	3.24
60	0.315	37.6	29.1	53.8	10.9	191.3	69.8	0.65	3.65
80	0.420	43.5	33.8	62.5	12.5	209.2	76.4	0.60	3.88
100	0.525	47.4	36.9	68.3	13.3	218.1	79.6	0.58	4.06
150	0.788	52.1	40.7	75.4	13.7	220.5	80.5	0.58	4.43

*As built. Hyd., hydraulic power; SEC_{el}, electrical specific energy (kWh/m³).

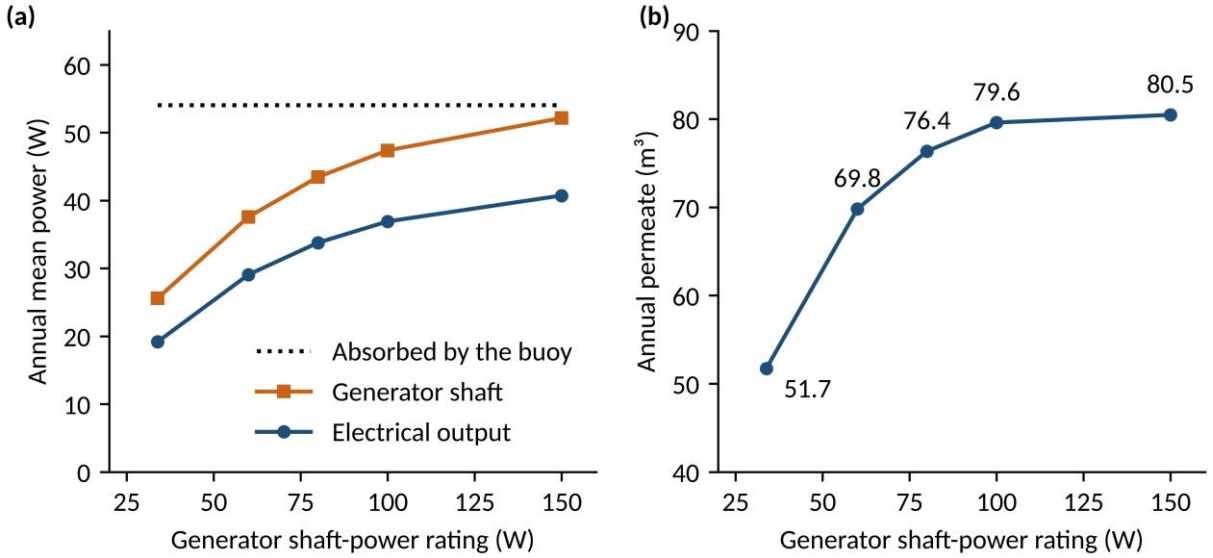


Fig. 11 Effect of the generator rating. (a) Annual mean power absorbed by the buoy (dotted), at the generator shaft and delivered as electricity. (b) Annual permeate. The first point is the as-built unit

5.9 Sensitivity to PTO inputs

Table 8 gives the sensitivity of the annual yield to the PTO inputs that were not varied in Section 5.6. Varying κ over the range of the four oscilloscope traces (0.251–0.269) changes the annual permeate by ±2.9%, and the 6 Ω exponent of 1.72 raises it by 7.1%; no ranking of the design levers changes. The force limit follows from the bench power, so it is covered by the 5.46% bench-power uncertainty (13% of the variance).

Table 8. Sensitivity of the annual yield (r = 0.3) to the PTO inputs; nominal 141.7 L/day, 0.83 g/L.

Input	Change	Permeate (L/day)	Salinity (g/L)	Change in yield
κ	0.251	137.6	0.85	−2.9 %
κ	0.269	145.8	0.81	+2.9 %
Power-law exponent n	1.72 (6 Ω fit)	151.8	0.79	+7.1 %

6 Discussion

6.1 Comparison with the literature

Table 9 places the results against published systems. The hydraulic specific energy of 1.23 kWh/m³ at 30% recovery and the electrical value of 3.24 kWh/m³ fall within the range of the best small systems and well below the 10–36 kWh/m³ for plants without energy recovery (Das et al. 2024). The electrical value is close to the 3.5 kWh/m³ that Thomson et al. reported for a kilowatt-scale system with energy recovery (Thomson et al. 2003), and slightly below the 4.5 kWh/m³ that Mi et al. projected for their direct hydraulic system at full-scale salinity (Mi et al. 2023). The modelled direct-drive batch system (Brodersen et al. 2022) reaches 2.3 kWh/m³ without the electrical chain and, as expected, lies below the figure for a chain with 85% conditioning and 48% motor–pump efficiency. The present unit passes 7.3 W through a 0.6 m² element, and the membrane runs at a low flux of about 10 L m^{-2} h^{-1}, well inside the range that Sitterley et al. found tolerable for fluctuating pressure (Sitterley et al. 2022).

Table 9. Comparison with published systems. SEC_h is counted at the membrane and SEC_{el} at the generator terminals (values as reported by the cited studies)

Study	System	Reported	This work
(Mi et al. 2023)	Hydraulic, piston pump and accumulator; scaled tank test	0.45 kWh/m³ in tank; 4.5 kWh/m³ projected at full scale	SEC_{el} 3.24 kWh/m³
(Das et al. 2024)	Wave-powered RO with energy recovery device	10–36 kWh/m³ without recovery	SEC_h 1.23 kWh/m³
(Brodersen et al. 2022)	Direct-drive batch RO, model	2.30 kWh/m³	SEC_h 1.23 kWh/m³
(Thomson et al. 2003)	Kilowatt-scale RO with energy recovery	3.5 kWh/m³	SEC_{el} 3.24 kWh/m³
(Sitterley et al. 2022)	Spiral-wound element, wave-driven pressure fluctuation, 1,770 h	Permeability −7.4%, rejection > 99%	Flux 8.8–11.0 L m^{-2} h^{-1}
(Elimelech and Phillip 2011)	Least work, seawater, r = 0.5	1.06 kWh/m³	1.056 (model)

6.2 Where the energy goes

The balance of Fig. 7 identifies three lossy stages. The first is the PTO rating. The generator, with a 60 W nameplate rating, limits the screw speed to 0.178 m/s, which caps the shaft power at 33.8 W, so that the buoy, which absorbs 54 W under the bench-derived force law, delivers only 25.6 W to the shaft. An idealised unconstrained linear damper (no torque or speed limit) of 1,650 N s/m would absorb 141.8 W in the same climate, a capture-width ratio of 4.79% and 2.6 times the current figure, so the buoy has substantial headroom for a larger generator rating or a staged torque law. Raising the generator shaft rating from 33.8 W to 100 W increases delivered power from 19.2 to 36.9 W and the annual permeate by 54% without changing the absorbed power (Section 5.8). The second is the motor–pump set, whose part-load efficiency of 48% is the largest uncertainty of the study and the first item worth improving, for instance with a pump matched to 15 W. The third is the conditioning stage, at 85%, where a direct DC drive of the motor could recover part of the loss. The membrane is not the bottleneck: the RO process reaches 72% of the least work, and membrane improvements would buy little.

6.3 Sizing and use

At 15 L/day per person for drinking, cooking and basic hygiene (Sphere 2018), one unit provides this volume for about nine people, and eleven units cover a village of one hundred. The batch cycle runs about 45,000 times a year, and a storage tank holding one day of yield (about 140 L) is sufficient to buffer the supply. The permeate salinity falls in the WHO fair taste band at r = 0.3, and a 0.3 m² membrane brings it to 0.50 g/L at a 15% higher energy cost, which is a useful option where taste matters. Yield varies by 1.2% between years, so supply varies little between years in a stationary climate. The upper-bound excitation case adds 17%, giving 166 L/day, which indicates the range that the calibration allows. Disinfection, remineralisation and microbiological safety are outside the model.

6.4 Limitations and scope

The results are a calibrated simulation and not a field measurement. The buoy excitation is calibrated to one published full-scale power, the PTO law is anchored to bench data up to 0.151 m/s and extended by 18% to the speed limit, and the torque limiter is a modelling assumption for the generator speed rating. The motor–pump efficiency curve is specified rather than measured, which is why it dominates the uncertainty (Fig. 9b). Each batch cycle runs at the mean hydraulic power of its sea state, and the model has no pre-treatment, fouling, brine-discharge or post-treatment stage; in a real unit the

brine, about 2.3 times the permeate volume at $r = 0.3$, returns to the sea through a diffuser, and pre-filtration, flushing and periodic membrane cleaning are needed. The PTO is assumed disengaged above 3 m. The permeate is characterised by its salinity, and potability needs disinfection and verification. The 1.2% interannual variation describes sampling of a stationary climate. The rating sweep and the linear-damper case are design scenarios for the model, not demonstrated performance. A sea trial of the complete unit would test each of these points. The batch-RO model has been checked for salt balance, pressure range and flux, but not against measurements, because no published data exist for a power-following batch unit of this size; it is therefore described as verified rather than validated.

6.5 Outlook

The simulation chain is verified on every link for which published data exist, and it yields a quantitative target for the next stage. A sea trial of the SB-1.5 unit with the PTO driving a small pump and a pressure vessel would measure the motor–pump map, the auxiliary loads and the absorbed power directly, and the three levers identified here, the PTO rating, the pump match and the recovery, can be tested in that campaign. The same chain applies to other sites by exchanging the climate matrix. A direct hydraulic drive comparison with the same buoy and assessment of levelised cost of water are beyond the scope of this study. Bench tests of a small batch-RO unit under variable power would supply the missing validation.

7 Conclusions

A verified S-shaped buoy and ball-screw PTO were coupled to a batch seawater RO model in a time-domain simulation of the ShiDao climate. The main conclusions are as follows.

- The unit absorbs 54.0 W of the 2,961 W of wave power over the buoy width (capture width ratio 1.83%). It delivers 19.2 W of electricity, with a capacity factor of 0.72 against the PTO rating.
- A batch cycle at 30% recovery turns 7.3 W of hydraulic power into 141.7 L/day (51.7 m^3/yr) at 0.83 g/L, with a hydraulic specific energy of 1.23 kWh/m^3, about 1.4 times the least work. The fixed-pressure once-through module gives 10.5 L/day on the same chain.
- The motor–pump set, at 48% stage efficiency, is the weakest link of the hydraulic side, and its efficiency explains 58% of the output variance. The 5–95% band of the annual yield is 115–171 L/day.
- The PTO rating limits the unit. An unconstrained linear damper would absorb 2.6 times more power, so a larger generator or a staged torque law is the principal route to higher yield. A 100 W generator delivers 99% of the yield of a 150 W unit and raises the as-built yield by a factor of 1.5.
- Higher recovery increases energy use and salinity; a larger membrane lowers energy use and raises salinity; and recirculation flow has an optimum at 3–4 L/min.
- One unit provides 15 L/day for about nine people, and eleven units for one hundred (volume only; potability needs post-treatment).

The energy balance gives the wave-energy and desalination communities a common ledger, and it identifies the PTO rating and the pump match as the priorities for a sea trial.

Statements and Declarations

Funding

This work was supported by the Guangdong Basic and Applied Basic Research Foundation (2025A1515012042), the GJYC program of Guangzhou (2024D03J0022), the Guangdong Innovation

and Entrepreneurship Team Project (2023ZT10H152), and the National Natural Science Foundation of China under Grant Nos. W2433151 (Project No. P110224G02012).

Competing interests.
The authors have no relevant financial or non-financial interests to disclose.

Ethics approval, consent to participate and consent for publication.
Not applicable. The study did not involve human participants or animals.

Data and code availability.
The experimental bench data used as model inputs (generator power, transmission efficiency, oscilloscope records) were published in the cited earlier papers (Ahmed et al. 2022, 2023b). The sea-state statistics were derived from measured records of Chinese coastal stations, as described in Section 2.3. The simulation scripts that support the figures and tables are available from the corresponding author upon reasonable request.

Author contributions
Ammar Ahmed: Conceptualization, Methodology, Software, Formal analysis, Data curation, Visualization, Funding acquisition, Writing - original draft. **Ali Azam:** Investigation, Formal analysis, Funding acquisition, Validation, Data curation, Writing - review & editing. **Zhichao Shen:** Supervision, Project administration, Resources, Funding acquisition, Writing - review & editing. **Xidong Zhou:** Software, Visualization, Writing - original draft. **Christopher N. Mkono:** Project administration, Resources, Writing - review & editing. **Zhongliang Meng:** Formal analysis, Data curation, Writing - review & editing. **Jakiya Sultana:** Data curation, Methodology, Writing - review & editing. **MD Mazedur Rahman:** Software, Visualization, Writing - review & editing. **Touqeer Aslam:** Investigation, Data curation, Visualization. **Dawood Majeed:** Investigation, Data curation, Visualization.

Use of AI tools
A large language model (Claude, Anthropic) was used to help develop and run the simulation scripts and for language editing. The authors designed the study, checked the results against the verification cases of Section 4, and take full responsibility for the content of the article.

References

Ahmed A, Azam A, Wang Y, et al (2023a) On the S-shaped floaters for a Wavestar-like wave energy converter with an I-shaped mechanical power take-off. Energy Conversion and Management: X 100387

Ahmed A, Azam A, Zhang Z, et al (2025) An isomorphic Froude scaling approach to bulbous-bottomed buoys in wave energy converters for smart floating cities. Applied Ocean Research 156:104485

Ahmed A, Wang Y, Azam A, et al (2023b) Design of an S-shaped point-absorber wave energy converter with a non-linear PTO to power the satellite-respondent buoys in the East China Sea. Ocean Engineering 275:114162

Ahmed A, Wang Y, Azam A, Zhang Z (2022) Design and analysis of the bulbous-bottomed oscillating resonant buoys for an optimal point absorber wave energy converter. Ocean Engineering 263:112443

Avalos GOG, Peña JCU, Rodríguez CLM (2024) Preliminary study of the performance of a new wave energy converter. Journal of Ocean Engineering and Marine Energy 10:125–136

Brodersen KM, Bywater EA, Lanter AM, et al (2022) Direct-drive ocean wave-powered batch reverse osmosis. Desalination 523:115393

Cotruvo JA (2017) 2017 WHO guidelines for drinking water quality: first addendum to the fourth edition. Journal-American Water Works Association 109:44–51

Cummins WE (1962) The impulse response functions and ship motion. Schiffstechnik 9:101–109

Das TK, Frost C, Folley M, Brewster P (2024) Application of an energy recovery device with RO membrane for wave powered desalination. Desalination 592:118064

Elimelech M, Phillip WA (2011) The future of seawater desalination: energy, technology, and the environment. Science 333:712–717

Falnes J, Kurniawan A (2020) Ocean waves and oscillating systems: linear interactions including wave-energy extraction. Cambridge university press

Folley M, Whittaker T (2009) The cost of water from an autonomous wave-powered desalination plant. Renewable Energy 34:75–81

Leijon J, Boström C (2018) Freshwater production from the motion of ocean waves–A review. Desalination 435:161–171

Li X, Chen C, Li Q, et al (2020) A compact mechanical power take-off for wave energy converters: Design, analysis, and test verification. Applied Energy 278:115459

Liang C, Ai J, Zuo L (2017) Design, fabrication, simulation and testing of an ocean wave energy converter with mechanical motion rectifier. Ocean Engineering 136:190–200

McLeod I, Ringwood J V (2022) Powering data buoys using wave energy: a review of possibilities. Journal of Ocean Engineering and Marine Energy 8:417–432

Mi J, Wu X, Capper J, et al (2023) Experimental investigation of a reverse osmosis desalination system directly powered by wave energy. Applied Energy 343:121194

Mithun SB, Remya PG, Sreejith M, et al (2025) Assessment of ocean wave energy potential and identification of technologically feasible hotspots for Indian coastal regions. Journal of Ocean Engineering and Marine Energy 11:1197–1220

Nakib TH, Hasanuzzaman M, Rahim NA, et al (2025) Global challenges of ocean thermal energy conversion and its prospects: a review. Journal of Ocean Engineering and Marine Energy 11:197–231

Nivetha K, Abdul Akbar M (2026) A state-of-the art review of heaving and pitching wave energy converters. Journal of Ocean Engineering and Marine Energy 12:1499–1524

Ola ATT, Heryanto H, Armynah B, Tahir D (2026) Development of renewable energy research using ocean waves: bibliometric analysis. Journal of Ocean Engineering and Marine Energy 12:519–534

Pitzer KS, Mayorga G (1993) Thermodynamics of electrolytes: II. Activity and osmotic coefficients for strong electrolytes with one or both ions univalent. In: Molecular structure and statistical thermodynamics: selected papers of Kenneth S Pitzer. World Scientific, pp 396–404

Saltelli A, Annoni P, Azzini I, et al (2010) Variance based sensitivity analysis of model output. Design and estimator for the total sensitivity index. Computer Physics Communications 181:259–270

Schock G, Miquel A (1987) Mass transfer and pressure loss in spiral wound modules. Desalination 64:339–352

Simmons JW, Van de Ven JD (2023) A comparison of power take-off architectures for wave-powered reverse osmosis desalination of seawater with co-production of electricity. Energies 16:7381

Sitterley KA, Cath TJ, Jenne DS, et al (2022) Performance of reverse osmosis membrane with large feed

pressure fluctuations from a wave-driven desalination system. Desalination 527:115546

Sphere S (2018) The Sphere Handbook: humanitarian charter and minimum standards in humanitarian response. 4th ed Geneva: Sphere Association

Thomson M, Miranda MS, Infield D (2003) A small-scale seawater reverse-osmosis system with excellent energy efficiency over a wide operating range. Desalination 153:229–236

Warsinger DM, Tow EW, Nayar KG, Maswadeh LA (2016) Energy efficiency of batch and semi-batch (CCRO) reverse osmosis desalination. Water Research 106:272–282

Wijmans JG, Baker RW (1995) The solution-diffusion model: a review. Journal of Membrane Science 107:1–21

Zolghadr M, Keshavarz Ab Pardeh P, Zomorodian SMA, Fathi A (2024) A laboratory study on paddle type wave energy converter for transferring seawater using wave energy. Journal of Ocean Engineering and Marine Energy 10:573–587